Hindawi
International Journal of Energy Research
Volume 2023, Article ID 6874429, 13 pages
https://doi.org/10.1155/2023/6874429

Research Article

Robust Core–Shell Carbon-Coated Silicon-Based Composite Anode with Electrically Interconnected Spherical Framework for Lithium-Ion Battery

A Hae Jo,[1,2] So Yeun Kim,[1] Ji Hoon Kim,[1] Yoong Ahm Kim,[2] and Cheol-Min Yang[1]

[1]*Institute of Advanced Composite Materials, Korea Institute of Science and Technology (KIST), Wanju-gun, Jeollabuk-do, Republic of Korea*
[2]*Department of Polymer Engineering, Graduated School, Chonnam National University, Gwangju, Republic of Korea*

Correspondence should be addressed to Cheol-Min Yang; cmyang1119@kist.re.kr

Received 10 October 2022; Accepted 25 October 2022; Published 3 February 2023

Academic Editor: Weiwei Han

Carbon-coated Si/carbon nanotube/graphene oxide (*C*-Si/CNT/GO) microspheres with a robust core–shell composite structure were successfully fabricated by efficient and scalable spray-drying and chemical vapor deposition (CVD) for application as a lithium-ion battery (LIB) anode. The amphiphilic GO nanoparticles facilitated the uniform dispersion of Si nanoparticles by suppressing the CNT aggregation in the Si/CNT/GO microspheres, efficiently forming a robust Si/CNT/GO microsphere composite structure. The surface of the Si/CNT/GO microsphere composite was coated with carbon using CH_4 via CVD to enhance its cycling performance. The four building block components, namely, Si nanoparticles, CNTs, and GO nanoparticles as the core and the carbon-coating layers as the shell, provided high electrochemical capacity, excellent electrical conductivity, efficient buffer space for the volume expansion of the Si nanoparticles, and high structural stability during lithiation/delithiation. The *C*-Si/CNT/GO composite anode also exhibited excellent electrochemical performance with high specific capacity (2921 mAh g^{-1} at 100 mA g^{-1}), long cycle life (1542 mAh g^{-1} at 200 mA g^{-1} after 100 cycles), and high charge/discharge rate (1506 mAh g^{-1} at 6 A g^{-1}). This approach for fabricating core–shell structured Si-based composite anodes with excellent electrochemical performance will provide a significant breakthrough for developing next-generation LIBs.

1. Introduction

With the increasing demand for electrochemical energy storage devices in range-extended electric vehicles (EVs), high-performance lithium-ion batteries (LIBs) with excellent energy density and cycling stability have gained immense interest in the scientific and industrial fields [1, 2]. To maximize the energy density of commercial LIBs, the most realistic approach is to improve the energy density of the electrode materials for LIBs [3–5]. Although graphite-based anode materials are commonly used in commercial LIBs, they show limited application as next-generation LIB anode materials owing to their low theoretical gravimetric and volumetric capacities for LiC_6 (372 mAh $g^{-1}$and 840 mAh cm^{-3}, respectively). Among the alloy-type anode materials, Si exhibits extremely high theoretical gravimetric and volumetric capacities of 3579 mAh g^{-1} and 2194 mAh cm^{-3}, respectively, upon lithiation to $Li_{15}Si_4$ phase. Hence, Si anodes have been widely suggested as promising alternatives to graphite-based anode materials. Furthermore, Si anodes have relatively low cost and average delithiation plateau and are environmentally friendly [6, 7]. Nevertheless, intense volume expansion and low intrinsic electrical conductivity of Si-based anodes lead to rapid capacity fading owing to cracking-induced pulverization and unstable solid–electrolyte interphase (SEI) layer formation [8].

Therefore, numerous engineering strategies have been developed to resolve these issues, and one of the strategies is to prepare composite structures of Si particles with electrically conductive carbonaceous materials (such as graphite [9, 10], pitch [11], carbon nanotubes (CNTs) [12, 13], and graphene [14, 15]). In particular, nanocarbon particles, such

as one-dimensional CNTs and two-dimensional graphene, with unique morphology, large and controllable specific surface area (SSA), excellent intrinsic electrical conductivity, superior chemical stability, and excellent mechanical flexibility, have been used to moderate the stress induced by volume expansion in Si-based anodes [16]. Moreover, nanocarbon particles act as effective electron transport pathways, significantly improving the cycling stability and charge/discharge rate of next-generation LIBs [17]. However, Si/nanocarbon composite anodes have some disadvantages. Several studies have indicated that the weak binding between the Si and nanocarbon particles during the cycling process is a major concern regarding Si/nanocarbon composite anodes since it leads to low cycling stability and capacity fading [18]. In addition, Si/nanocarbon composite anodes suffer from poor rate capability because of the bundling or aggregation caused by the strong van der Waals interactions during mixing and casting, resulting in an electrical disconnection between the Si and nanocarbon particles [19].

Generally, the water solubility of CNTs is improved by adding a surfactant or employing an oxidation treatment in a mixed acid solution. However, these methods considerably decrease the electrical conductivity of the CNTs owing to the presence of a residual surfactant or the formation of surface defects [20]. Therefore, an effective method must be adopted to disperse CNTs in an aqueous solution without adding a surfactant and forming defects on the CNT surface. Graphene oxide (GO) nanoparticles prepared by the mechanical exfoliation of oxidized graphite have been used to enhance the dispersibility of CNTs in aqueous solutions [21]. The amphiphilic GO nanoparticles show a strong affinity for hydrophilic water molecules and hydrophobic CNTs, thus facilitating the formation of a stable CNT dispersion in CNT/GO aqueous solutions [22, 23]. Therefore, Si nanoparticles can be uniformly dispersed by suppressing the aggregation of CNTs in Si/CNT/GO composites using GO nanoparticles. Moreover, Si/CNT/GO composites are expected to show synergistic effects by utilizing the advantages of the CNT and GO components.

Thus, regarding the LIB technology, the present study is aimed at developing a simple yet effective synthesis technique that can yield homogeneously mixed Si/nanocarbon composite anode material suitable for improved electrochemical performances. This study reports the utilization of a novel electrically conductive spherical framework composed of uniformly dispersed CNT and GO components without any posttreatment, such as chemical surface modification, centrifugation, and surfactant as a Si-based LIB anode material. A novel Si/CNT/GO microsphere composite anode with a three-dimensional (3D) architecture was designed and optimized using a spray-drying process to improve the electrochemical performances of LIBs effectively. The surface of the Si/CNT/GO microsphere was coated with carbon using CH_4 via chemical vapor deposition (CVD) to enhance the electrochemical cyclic stability of the composite anode (*C*-Si/CNT/GO). Subsequently, the electrochemical characteristics of the *C*-Si/CNT/GO composite anode were investigated to confirm the synergistic effects of the nanoparticles constituting the composite material and its possible application as a LIB anode. The results demonstrated the potential application of the Si-based composite anode for a high-performance LIB.

2. Experimental

2.1. Materials and Preparation of Composites. GO nanoparticles were synthesized from graphite (325 mesh, Alfa Aesar, USA) using a Couette–Taylor flow reactor according to the modified Hummers method [24, 25]. Multi-walled CNTs (CM-280) were purchased from Hanwha Chemical, Korea. Three different solutions and Si-based composites were prepared as follows: (a) CNTs (0.5 g) were dispersed and stirred in deionized water (300 mL) for 0.5 h and then ultrasonicated for 6 h to prepare solution A. The CNTs were used without posttreatment to avoid deterioration of their electrical conductivity. (b) GO nanoparticles (0.5 g) were added to solution A and then ultrasonicated for 2 h to prepare solution B. (c) Sodium dodecyl benzene sulfonate (SDBS) surfactant (0.5 g) was added to solution A and subsequently ultrasonicated for 2 h to prepare solution C. (d) Si nanoparticles (<100 nm, Alfa Aesar, USA) (2.5 g) were added to solutions A, B, and C and then ultrasonicated for 2 h (Si/CNT/GO weight ratio = 5 : 1 : 1) to fabricate Si-based composites. Subsequently, the as-obtained solutions were spray-dried to form a spherical composite structure [26]. Finally, the spray-dried samples were freeze-dried, and the resulting composite samples obtained from solutions A, B, and C were labeled as Si/CNT, Si/CNT/GO, and Si/CNT/(*S*), respectively. (e) The CVD treatment using CH_4 gas was performed in a horizontal tube furnace to fabricate carbon-coated Si-based composites [11]. The composites were heat-treated to 760°C (5°C min^{-1} rate, Ar atmosphere); this temperature was maintained in a precursor gas atmosphere of Ar and CH_4 (200 sccm) for 1 h. The CVD-treated composites were denoted as *C*-Si/CNT, *C*-Si/CNT/GO, and *C*-Si/CNT/(*S*). (f) For comparison, the Si/CNT, Si/CNT/GO, and Si/CNT/(*S*) composites were heat-treated to 760°C (5°C min^{-1} rate) and maintained at 760°C (1 h) in an Ar atmosphere (200 sccm). The heat-treated composites were referred to as *H*-Si/CNT, *H*-Si/CNT/GO, and *H*-Si/CNT/(*S*). The schematic for the preparation of the composites is shown in Figure 1.

2.2. Characterization. Field-emission scanning electron microscopy (FE-SEM; Nova NanoSEM 450, FEI, USA) and high-resolution transmission electron microscopy (HR-TEM; Tecnai G2 F20, FEI, USA) were performed to observe the morphologies and microstructures of the composite materials; cross-sectional specimens were prepared using an Ar-ion beam polisher. X-ray diffraction (XRD), Raman, and X-ray photoelectron spectroscopy (XPS) analyses of the composites were performed using an X-ray diffractometer (Cu K_α radiation of 0.154 nm wavelength, SmartLab, Rigaku, Japan), an Ar-ion laser (514 nm wavelength and 20 mW power, inVia Reflex Raman microscope, Renishaw, USA), and a monochromatic Al-K_α X-ray source (15 mA, 14 kV, K-Alpha instrument, Thermo Scientific, USA), respectively. Thermogravimetric analysis (TGA) was performed in the temperature range of 25–1000°C (5°C min^{-1}

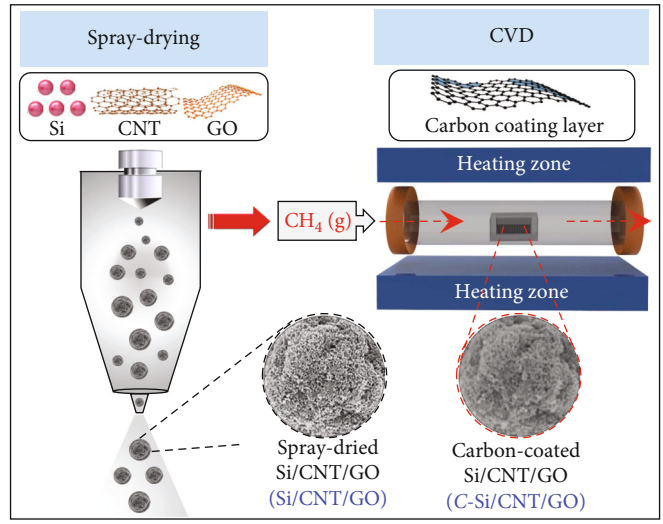

FIGURE 1: Schematic illustration of the preparation process of the *C*-Si/CNT/GO microsphere composite by spray-drying and subsequent CVD.

rate, air atmosphere) (Q50, TA Instruments, USA). The SSAs of the samples were determined using the Brunauer–Emmett–Teller (BET) equation from their N_2 adsorption isotherms (−196°C) measured using a volumetric-type equipment (BELSORP-max, MicrotracBEL, Japan).

2.3. Cell Fabrication and Electrochemical Analyses. The working electrodes were fabricated by mixing the composites (80 wt%), carbon black (Super-P, 10 wt%), and polyacrylic acid (10 wt%) as the active material, conducting agent, and binder, respectively, in deionized water. The slurries were coated on a Cu foil, dried in a vacuum oven (120°C, 12 h) to remove the solvent completely, and pressed (200 kg cm^{-2}). The performance of the electrodes was compared by fixing the electrode material thickness at 25 μm (loading amount of approximately 1–2 mg cm^{-2}). Coin-type half-cells (CR2032) were assembled using a separator (polyethylene membrane) and an electrolyte (1 M Li hexafluorophosphate ($LiPF_6$) solution in a mixture of ethylene carbonate and dimethyl carbonate (3 : 7 *v*/*v*, Panax Etec Co. Ltd., Korea)). The electrochemical performance was evaluated by performing galvanostatic charge (Li-ion insertion) and discharge (Li-ion extraction) (GCD) measurements at a current rate of 0.1 C (100 mA g^{-1}) in the potential range of 0.01–2.0 V vs. Li/Li$^+$ (WBCS3000, WonATech, Korea). Cyclic voltammetry (CV) and electrochemical impedance spectroscopy (EIS) data were obtained at a scan rate of 0.1 mV s^{-1} and in the frequency range of 100 kHz–0.01 Hz, respectively, using an electrochemical workstation (ZIVE SP2, WonATech, Korea). The surface electrical conductivities of the composite anodes were measured using the four-point probe technique (FPP-RS8, Dasol Eng., Korea) [27].

3. Results and Discussion

The fabrication procedure of the Si/CNT/GO microsphere composites with a diameter of several micrometers is schematically shown in Figure 1. The microsphere composites were composed of Si nanoparticles, CNTs, and GO nanoparticles as the main building blocks. GO nanoparticles were used as a dispersion agent to facilitate the dispersion of CNTs and Si nanoparticles in the mixed aqueous solution. During the spray-drying process, the Si nanoparticles, CNTs, and GO nanoparticles were assembled into microspheres with a 3D framework, which was composed of agglomerated CNTs entangled with each other and Si/GO nanoparticles dispersed in the CNT matrix structure (Si/CNT/GO). After the subsequent CVD process using CH_4 gas at 760°C, a core–shell structure was formed with the Si/CNT/GO microspheres (core) and a carbon-coating layer (shell) (*C*-Si/CNT/GO). The thermal annealing effect during the CVD process reduced the GO nanoparticles. The carbon-coating layer of the microspheres improved the electrical conductivity, prevented electrolyte permeation, and suppressed the side reactions and SEI formation. Moreover, the CVD treatment of the microspheres enabled tight binding of the three types of nanomaterials, which improved the mechanical structural stability of the microspheres.

For the *H*-Si/CNT/GO and *C*-Si/CNT/GO composites, the morphologies were compared using FE-SEM and HR-TEM (Figure 2). The Si nanoparticles, CNTs, and GO nanoparticles aggregated to form a spherical structure (diameter of approximately 5–10 μm) during the spray-drying process (Figure 2(a)). No significant changes in the spherical morphology and average diameter of the Si/CNT/GO composite were observed after the CVD treatment, while the deposited carbon smoothened the rough surface of the microspheres (Figure 2(b)). The magnified FE-SEM image showed the presence of Si nanoparticles, CNTs, and GO nanoparticles on the Si/CNT/GO microsphere surface (inset of Figure 2(a)). In contrast, the surface of the *C*-Si/CNT/GO microspheres exhibited a denser microstructure (inset of Figure 2(b)), which is associated with the effect of the carbon-coating layer. The HR-TEM image of the *C*-Si/CNT/GO microsphere showed that the CNTs were tightly entangled or aligned into the porous

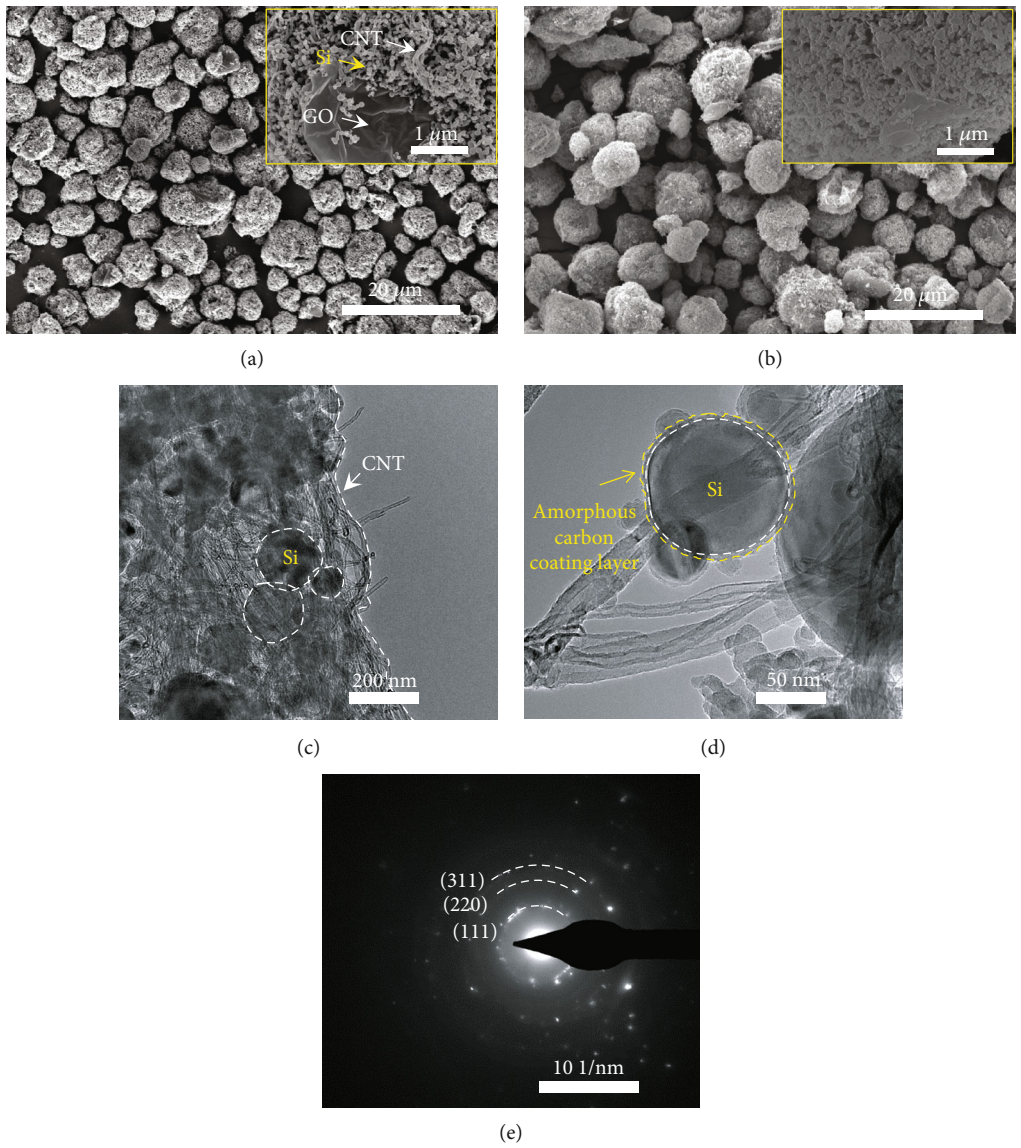

Figure 2: FE-SEM images of (a) *H*-Si/CNT/GO and (b) *C*-Si/CNT/GO microsphere composites (insets are the high-resolution images of the microsphere surfaces). (c, d) HR-TEM images of the *C*-Si/CNT/GO microsphere composite at different magnifications and (e) the corresponding SAED pattern.

microspheres, and the Si nanoparticles were anchored in the CNT network (Figure 2(c)). Additionally, the magnified HR-TEM image confirmed that the Si nanoparticles were coated with an amorphous carbon layer (approximately 5 nm thickness) (Figure 2(d)). However, the carbon layers coated on the microsphere surface were not observed using HR-TEM, which is consistent with a previous study [11]. This composite structure showed improved electron transfer ability and effectively buffered the lithiation-induced volume expansion of Si, facilitating the stable SEI layer formation and preventing the loss of electrical contacts. The selected area electron diffraction (SAED) pattern corresponding to the HR-TEM image confirmed the fine crystal structure of the Si nanoparticles (Figure 2(e)). The diffraction rings in the SAED pattern are assigned to the (111), (220), and (311) planes of crystalline Si [28], which was further confirmed by the XRD analysis results. Conversely, the *C*-Si/CNT and *C*-Si/CNT/(*S*) composites exhibited doughnut-like morphology (Figure S1), indicating that the microsphere structure was unsuccessfully formed in these composites during the spray-drying process. This result suggests that the GO nanoparticles played a vital role in the formation of the spherical morphology by controlling the dispersibility of the CNTs and demonstrating excellent sphere-forming ability of the GO nanoparticles during the spray-drying process [25].

The crystal structures and compositions of the carbon-coated composites were analyzed using XRD. The XRD patterns exhibited sharp peaks at $2\theta = 29^\circ$, 47°, 56°, 69°, and 77°, indicating crystalline Si (Figure 3(a)) [29], while the weak and broad peaks at $2\theta = 26^\circ$ are attributed to the (002) plane of the carbonaceous materials [30]. The XRD peak of the *C*-Si/CNT/(S) composite that appeared at approximately

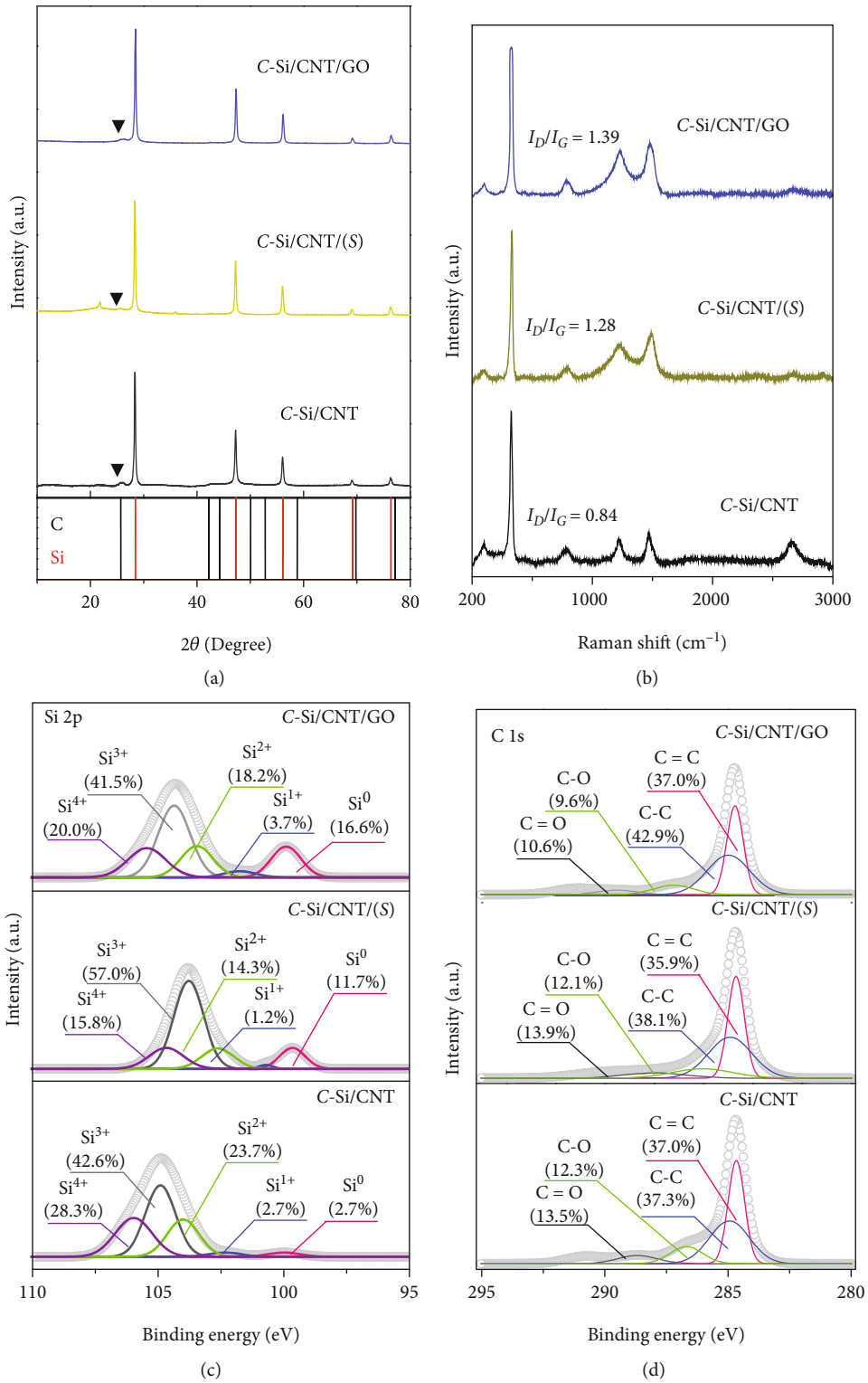

Figure 3: (a) XRD patterns, (b) Raman spectra, (c) deconvoluted Si 2p XPS profiles calibrated against the C 1s peak at 284.5 eV, and (d) deconvoluted C 1s XPS profiles of the *C*-Si/CNT, *C*-Si/CNT/(*S*), and *C*-Si/CNT/GO composites.

22° is ascribed to the presence of residual SDBS surfactant that was used in the synthesis. The compositions of the composites were also analyzed using the Raman spectroscopy (Figure 3(b)). The Raman spectra showed three peaks at approximately 295, 510, and 950 cm^{-1}, indicating crystalline Si [31]. The two broad peaks at approximately 1350 cm^{-1} (disordered structure, D-band) and 1580 cm^{-1} (graphitic structure, G-band) are the characteristic of carbonaceous materials, such as CNTs, GO nanoparticles, and carbon-coating layers [32]. Therefore, the concentration of structural

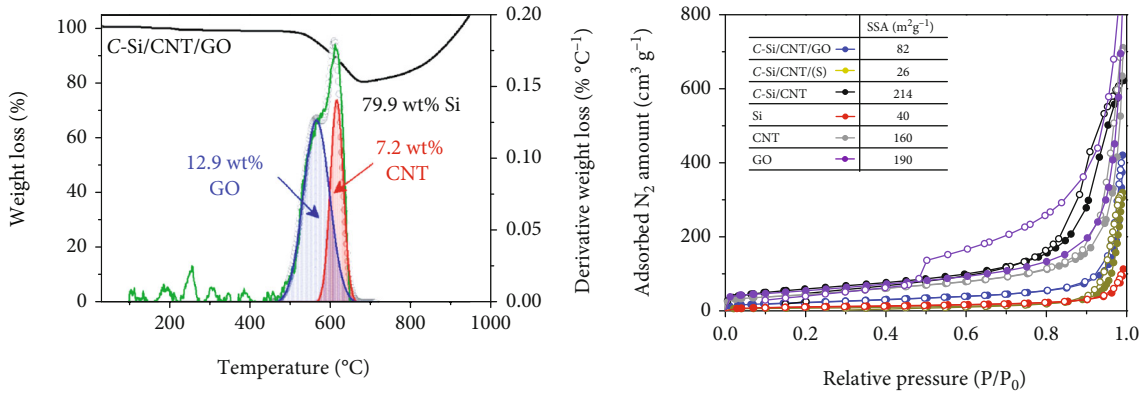

(a) (b)

Figure 4: (a) TGA and deconvoluted DTGA curves of the *C*-Si/CNT/GO microsphere composite in an air atmosphere. (b) N_2 adsorption isotherms (−196°C) of the *C*-Si/CNT, *C*-Si/CNT/(*S*), and *C*-Si/CNT/GO composites and the nanoparticles (Si, CNT, and GO) constituting the composite materials. The inset shows the SSAs calculated using the BET method.

Table 1: Electrochemical properties and sheet resistances of the *C*-Si/CNT, *C*-Si/CNT/(*S*), *H*-Si/CNT/GO, and *C*-Si/CNT/GO composite LIB anodes.

Sample	Charge capacity after 1 cycle (mAh g^{-1})	Discharge capacity after 1 cycle (mAh g^{-1})	Initial Coulombic efficiency after 1 cycle (%)	Capacity retention after 50 cycles (mAh g^{-1})	Capacity retention after 100 cycles (mAh g^{-1})	Sheet resistance (mΩ sq^{-1})
C-Si/CNT	647	317	49	191	196	1.50
C-Si/CNT/(*S*)	1675	1273	76	899	423	1.16
H-Si/CNT/GO	2970	2436	82	1393	—	—
C-Si/CNT/GO	2921	2395	82	1785	1542	0.87

defects in the carbonaceous materials was analyzed using the I_D/I_G ratio. The I_D/I_G ratio was the highest at 1.39 for *C*-Si/CNT/GO composite, which originated from a more defective GO component in the *C*-Si/CNT/GO composite.

The surface chemical compositions of the carbon-coated composites were investigated using XPS, which indicated the presence of Si, C, N, and O (Figure S2). The Si contents on the surfaces of the composites were 29.2 (*C*-Si/CNT), 18.5 (*C*-Si/CNT/(*S*)), and 22.6 at % (*C*-Si/CNT/GO) (Table S1). *C*-Si/CNT/(*S*) showed a Na 1s peak (1.7 at %) at 1072 eV owing to the residual SDBS surfactant [33]. Furthermore, all the Si 2p XPS spectra were deconvoluted into five peaks at approximately 99.9, 101.8, 103.5, 104.4, and 105.4 eV, which corresponded to elemental Si^0, Si^{1+}, Si^{2+}, Si^{3+}, and Si^{4+}, respectively (Figure 3(c)) [34, 35]. The fractions of elemental Si^0 in the total Si content of the composites were 2.72 (*C*-Si/CNT), 11.7 (*C*-Si/CNT/(*S*)), and 16.6% (*C*-Si/CNT/GO). The Si 2p XPS profile of the *C*-Si/CNT/GO composite indicated the preservation of the crystalline Si structure during the fabrication process. All the C 1s XPS spectra were deconvoluted into four peaks at approximately 284.6, 285.2, 286.8, and 288.9 eV, which corresponded to C=C, C–C, C–O, and C=O bonds, respectively (Figure 3(d)) [36]. The *C*-Si/CNT/GO composite exhibited a C=C to C–C ratio of 0.86, which was lower than that of *C*-Si/CNT(*S*) (0.94) and *C*-Si/CNT (0.99). This observation is associated with the more defective GO component in the *C*-Si/CNT/GO composite.

Additionally, the compositions of the carbon-coated composites were confirmed by obtaining their TGA and derivative TGA (DTGA) curves in an air atmosphere (Figure 4(a) and Figure S3). The estimated Si contents were approximately 87.9 (*C*-Si/CNT), 88.8 (*C*-Si/CNT/(*S*)), and 79.9 wt% (*C*-Si/CNT/GO) (Figure S3 and Table S2). The total Si content for all the composite samples obtained by TGA was significantly higher than the surface Si content obtained by the XPS technique, which is attributed to the core–shell composite structure of the carbon-coating layers on the outer surface and the embedded Si nanoparticles in the inner space of the microsphere composites, respectively. The TGA curve of the *C*-Si/CNT/GO composite exhibited a strong weight loss peak at 450 −650°C due to the thermal-oxidative decomposition of the CNT and GO structures. The weight increase over 650°C was attributed to the formation of SiO_2 by the oxidation of the Si nanoparticles. The CNT and GO contents of the *C*-Si/CNT/GO composite were approximately 7.2 and 12.9 wt%, respectively, which were obtained by deconvoluting the DTGA curve of the *C*-Si/CNT/GO composite (Figure 4(a)).

The SSAs of the carbon-coated composites and nanoparticles (Si nanoparticles, CNTs, and GO nanoparticles) constituting the composites were determined by the N_2 adsorption technique. Figure 4(b) shows the N_2 adsorption isotherms (−196°C) of the composites, their components, and the corresponding BET SSAs. The Si nanoparticles and

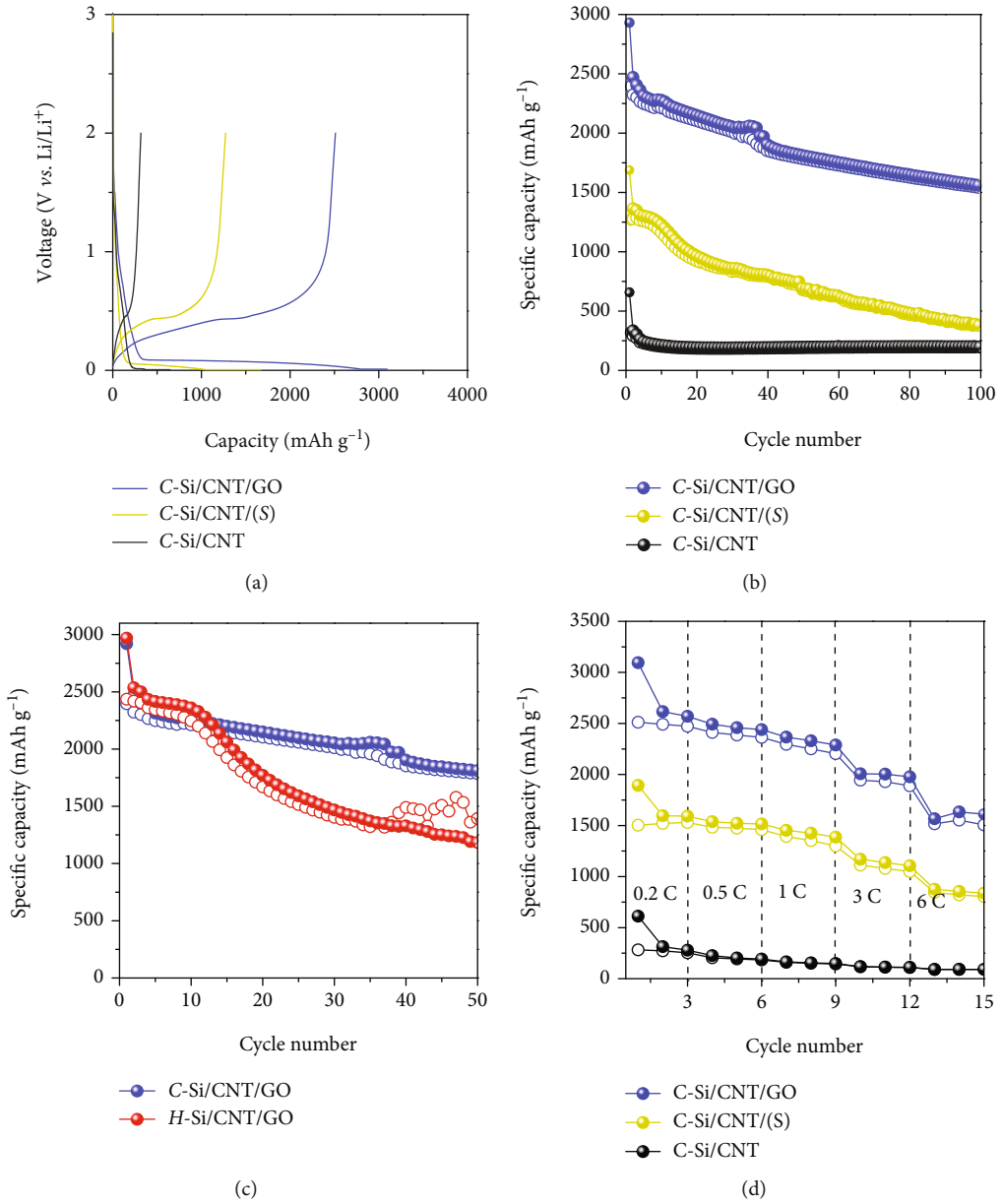

Figure 5: Continued.

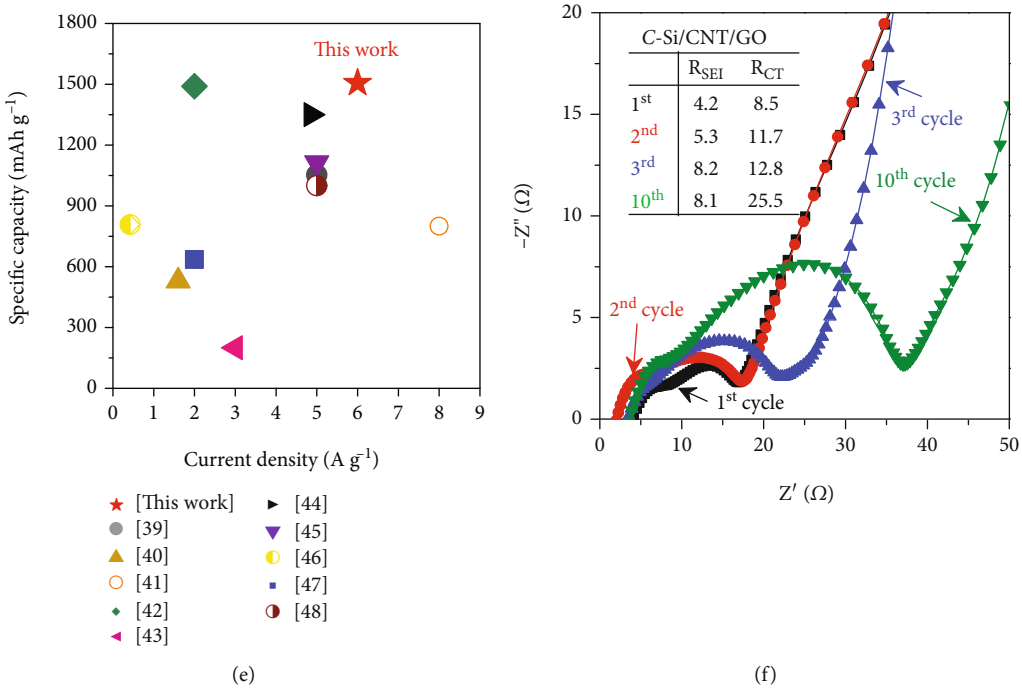

FIGURE 5: Electrochemical performances of the *C*-Si/CNT, *C*-Si/CNT/(*S*), *H*-Si/CNT/GO, and *C*-Si/CNT/GO composite anodes. (a) GCD profiles during the first cycle between 0.01 and 2.0 V vs. Li/Li^+ at a rate of 0.1 C (100 mA g^{-1}). (b, c) Cyclic performances at a rate of 0.2 C (200 mA g^{-1}) and 0.01–2.0 V vs. Li/Li^+ for 100 cycles. (d) Rate capabilities at various rates of 0.2, 0.5, 1, 3, and 6 C. (e) Specific capacities of the *C*-Si/CNT/GO composite anode prepared in this study and the previously reported Si/CNT/graphene composite anodes. (f) The Nyquist plots and resistance values of the *C*-Si/CNT/GO composite anode after the first, second, third, and tenth cycles at 6 A g^{-1}.

CNTs exhibited type-II N_2 adsorption isotherms, whereas the GO nanoparticles exhibited type-IV with a wide H3-type hysteresis loop, which is ascribed to the slit-shaped pores between the flake-like GO sheets. The increased amounts of adsorbed N_2 for the nanoparticles at medium and high relative pressures (P/P_0) are attributed to the multimolecular layer adsorption on the interstitial pores and the external surface between the nanoparticles; the SSAs of the Si nanoparticles, CNTs, and GO nanoparticles were 40, 160, and 190 $m^2 g^{-1}$, respectively. The composites exhibited type-II N_2 adsorption isotherms, indicating that they mainly consisted of meso-/macropores; the SSAs of the composites were 214 (*C*-Si/CNT), 26 (*C*-Si/CNT/(*S*)), and 82 $m^2 g^{-1}$ (*C*-Si/CNT/GO). The relatively high SSA of the *C*-Si/CNT composite is attributed to the bundled or entangled CNTs due to their poor dispersibility, which resulted in the exposure of many Si nanoparticles on the surface of the composite. Thus, controlling the volume expansion of Si nanoparticles is difficult in this composite structure. Conversely, the *C*-Si/CNT(*S*) and *C*-Si/CNT/GO composites exhibited more packed structures due to the well-dispersed CNTs. In particular, the meso-/macropores of the *C*-Si/CNT/GO composite provided a structural buffer space to withstand the volume expansion of the well-dispersed Si nanoparticles into the CNT/GO spherical framework during the repeated lithiation/delithiation reactions, thereby preventing the cracking-induced pulverization of the Si-based anode and improving its cyclic stability. The electrical conductivity of the *C*-Si/CNT/GO composite anode was higher than that of the *C*-Si/CNT and *C*-Si/CNT/(*S*) composite anodes (Table 1). Therefore, for the *C*-Si/CNT/GO composite anode, the spherical framework composed of CNTs and GO nanoparticles as a carbonaceous matrix provided enhanced electrical conductivity because of its low contact resistance and excellent structural stability against the Li-ion insertion-induced volume expansion.

Figure 5(a) illustrates the GCD profiles of the carbon-coated composite anodes during the first cycle over the potential range of 0.01–2.0 V vs. Li/Li^+ and at a rate of 0.1 C (100 mA g^{-1}). A long plateau was observed for all composite anodes at approximately 0.1 V in the first charging curve due to the formation of amorphous Li_xSi during the lithiation process. The charge capacities of the carbon-coated composite anodes after the first cycle were 647 (*C*-Si/CNT), 1675 (*C*-Si/CNT/(*S*)), and 2921 mAh g^{-1} (*C*-Si/CNT/GO), and the corresponding initial Coulombic efficiencies were 49, 76, and 82%, respectively (Table 1). The initial Coulombic capacity of the *C*-Si/CNT/GO composite anode was superior to that of the Si/CNT/(*S*) and *C*-Si/CNT composite anodes. This result suggests that the GO nanoparticles acted as a bridge to connect the Si nanoparticles mechanically and electrically in the composite anode structure during the lithiation/delithiation reactions. Moreover, the low initial Coulombic efficiency of the *C*-Si/CNT anode is attributed to the aggregation of the CNTs due to their poor dispersibility in the aqueous solution, which resulted in the low electrical conductivity of the anode.

The Li-ion storage behavior of the *C*-Si/CNT/GO composite anode was investigated by conducting CV measurements over the potential range of 0.01–2.0 V for three

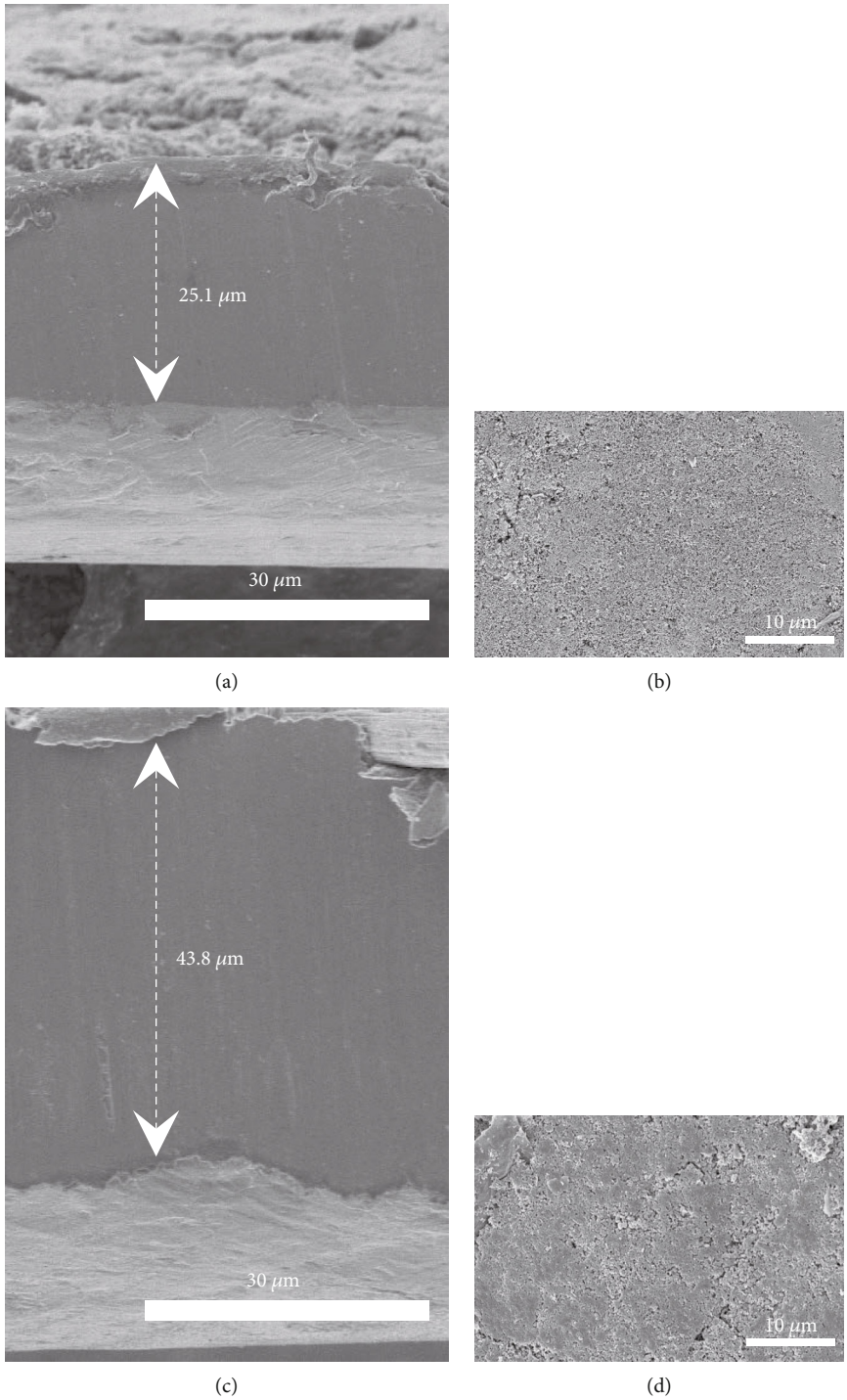

Figure 6: (a, c) Cross-sectional and (b, d) top-view FE-SEM images of the *C*-Si/CNT/GO microsphere composite anode (a, b) before and (c, d) after 100 cycles.

cycles (Figure S4A). During the charging process, a sharp reduction peak was observed below 0.1 V, indicating the insertion of Li-ions into the polycrystalline Si and the formation of amorphous Li_xSi [37]. In the discharging process, two broad oxidation peaks were observed at 0.35 and 0.51 V, suggesting the decomposition of Li_xSi and delithiation from Si, respectively. In the subsequent cycles, the cathodic peak intensity at 0.2 V gradually increased owing to the formation of the Li–Si alloy phase. In addition, the intensities of the cathodic and anodic peaks increased during the cycling process, indicating the activation of more Si phases during the charging/discharging processes. The peaks in the differential capacity plots of the composite anodes are attributed to the phase changes caused by the electrochemical reactions, which is consistent with the CV results (Figure S4B).

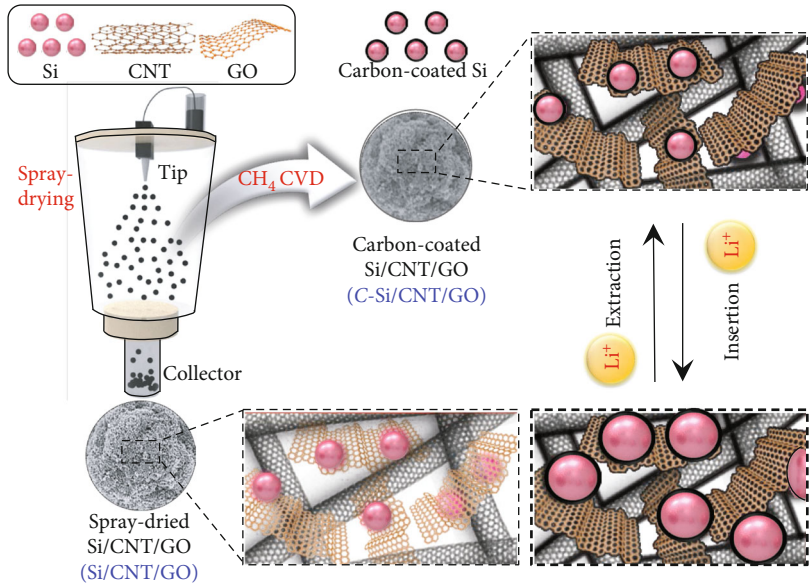

FIGURE 7: Schematic showing the structural changes in the *C*-Si/CNT/GO microsphere composite anode after the lithiation/delithiation processes.

Figure 5(b) shows the cycle performances of the carbon-coated composite anodes at a rate of 0.2 C (200 mA g^{-1}). After 100 cycles, the specific capacity of the *C*-Si/CNT/GO composite anode was maintained at 1542 mAh g^{-1} (64% capacity retention), while that of the *C*-Si/CNT and *C*-Si/CNT/(*S*) composite anodes decreased to 196 (62% capacity retention) and 423 mAh g^{-1} (33% capacity retention), respectively (Table 1). After 200 cycles, the *C*-Si/CNT/GO composite anode continued to exhibit superior capacity retention than the *C*-Si/CNT and *C*-Si/CNT/(*S*) composite anodes (Figure S5). The cycle performances of *H*-Si/CNT/GO and *C*-Si/CNT/GO were compared (up to 50 cycles) to confirm the effect of the carbon coating on the cycle performance of the composite anodes (Figure 5(c)). The specific capacity of the *H*-Si/CNT/GO composite anode drastically decreased from 2436 to 1393 mAh g^{-1} after 50 cycles. This result indicates that the *H*-Si/CNT/GO composite anode showed capacity retention of 57%, which can mainly be attributed to the volume expansion due to the formation of Li_xSi during the continuous charging/discharging processes (Figure 5(c)) [38]. The capacity retention (after 50 cycles) of the *C*-Si/CNT/GO composite anode (75%) was significantly higher than that of the *H*-Si/CNT/GO composite anode (57%). The carbon-coating layers in the *C*-Si/CNT/GO composite acted as electrical bridges between the neighboring Si nanoparticles, CNTs, and GO nanoparticles to form effective electron transfer pathways. Moreover, these layers facilitated the formation of a mechanically robust *C*-Si/CNT/GO composite structure. The rate capabilities of the composite anodes are shown in Figure 5(d). The *C*-Si/CNT/GO composite anode exhibited improved rate capability and cycle stability than the *C*-Si/CNT and *C*-Si/CNT/(*S*) composite anodes. For Li-ion extraction up to 6 C, the *C*-Si/CNT/GO composite anode exhibited an excellent rate capability of 1506 mAh g^{-1}, which was compared with the rate capability of previously reported Si/CNT/graphene composite anodes (Figure 5(e)) [39–48]. The *C*-Si/CNT/GO composite anode fabricated in this study exhibited a rate capability superior to that of other Si/CNT/graphene composite anodes, even at high current densities. Figure 5(f) illustrates the Nyquist plots and resistance values for the *C*-Si/CNT/GO composite anode at 6 A g^{-1} after the first, second, third, and tenth cycles. The interfacial resistance (R_{SEI}) and charge transfer resistance (R_{CT}) values of the *C*-Si/CNT/GO composite anode were 4.2 and 8.5 Ω, respectively [49, 50]. The R_{SEI} and R_{CT} values increased with the number of charge–discharge cycles. However, the R_{SEI} value did not increase further after the third cycle, indicating the effective formation of the SEI layer during the 3-cycle charge–discharge process.

The changes in the morphology of the *C*-Si/CNT/GO composite anode after the charging/discharging processes were investigated to confirm its structural stability. Figure 6 shows the cross-sectional and top-view FE-SEM images of the *C*-Si/CNT/GO composite anode before and after 100 cycles. The anode samples were cross-sectioned using an Ar-ion beam polisher for the cross-sectional observation. The *C*-Si/CNT/GO composite anode (thickness of 25.1 μm) exhibited a low volume expansion ratio of 74.5% after 100 cycles. Furthermore, the cycled *C*-Si/CNT/GO composite anode did not exhibit any significant disintegration, such as microscale cracks and the delamination of the anode materials from the current collector. This phenomenon is attributed to the high electrical conductivity and sufficient buffer space of the interconnected CNT framework of the composite anode (Figure 7). Moreover, the GO nanoparticles and carbon-coating layers interlaced with the CNT network provided mechanical stability for the volume expansion of the embedded Si nanoparticles and electrically conductive channels (Figure 7).

4. Conclusion

A carbon-coated Si/CNT/GO microsphere composite was successfully fabricated using efficient and industrially scalable spray-drying and CVD processes for application as a high-performance LIB anode material. The *C*-Si/CNT/GO composite anode exhibited excellent electrochemical performance with high specific charge and discharge capacities (2921 and 2395 mAh g^{-1} at 100 mA g^{-1}, respectively), long cycle life (1542 mAh g^{-1} at 200 mA g^{-1} after 100 cycles, capacity retention of 64%), and high charge/discharge rates (1506 mAh g^{-1} at 6 A g^{-1}). The components of the *C*-Si/CNT/GO composite anode had a synergistic effect on its electrochemical performance for LIB applications (Figure 7). The Si nanoparticles, CNTs, GO nanoparticles, and carbon-coating layers contributed to the excellent electrochemical performance of the *C*-Si/CNT/GO composite as a LIB anode. The possible contributions are as follows: (a) the Si nanoparticles contributed to the high electrochemical capacity of the *C*-Si/CNT/GO composite; (b) the CNTs facilitated the formation of the electrical networks and spherical frameworks, depending on the dispersibility of the CNTs, and thus, the well-dispersed CNTs improved the electrical conductivity of the 3D architecture and provided sufficient buffer space for accommodating the volume expansion of the Si nanoparticles; (c) the GO nanoparticles enabled the formation of electrically conductive pathways and played a vital role in the formation of spherical morphology by the suspension of CNTs in the aqueous Si/CNT/GO dispersion, which was promoted by the excellent sphere-forming ability of the GO nanoparticles during the spray-drying process [25, 51]; and (d) furthermore, the carbon-coating layer improved the electrical conductivity and mechanical structural stability of the composite, prevented electrolyte permeation, and suppressed the side reactions and SEI formation [52]. Our study reveals that the electrically interconnected carbonaceous framework significantly enhances the buffering effect for volume expansion and the Li-ion diffusivity in the Si-based composite anode, which is associated with the robust framework and increased diffusion channels by synergistic effects of the uniformly dispersed CNTs and GO nanoparticles and the carbon-coating layers. We expect that our efficient and scalable method for producing robust Si-based core–shell composite anodes can provide a significant breakthrough for developing next-generation LIBs for EVs.

Data Availability

The additional data used to support the findings of this study are included within the supplementary information file.

Conflicts of Interest

The authors declare that they have no conflicts of interest.

Authors' Contributions

A Hae Jo and So Yeun Kim contributed equally to this work.

Acknowledgments

This research was supported by the Korea Institute of Science and Technology (KIST) Institutional Program.

Supplementary Materials

FE-SEM images (Figure S1), XPS profiles (Figure S2), and TGA curves (Figure S3) of the composites. CV curves (Figure S4) and cyclic performances (Figure S5) of the composite anodes. Elemental compositions (Table S1) and residual amounts (Table S2) of the composites. This supplementary material can be found online in the Supporting Information section at the end of this article. *(Supplementary Materials)*

References

[1] G. Zubi, R. Dufo-López, M. Carvalho, and G. Pasaoglu, "The lithium-ion battery: state of the art and future perspectives," *Renewable and Sustainable Energy Reviews*, vol. 89, pp. 292–308, 2018.

[2] K. Liu, Y. Liu, D. Lin, A. Pei, and Y. Cui, "Materials for lithium-ion battery safety," *Science Advances*, vol. 4, no. 6, p. eaas9820, 2018.

[3] X. Shen, H. Liu, X.-B. Cheng, C. Yan, and J. Q. Huang, "Beyond lithium ion batteries: higher energy density battery systems based on lithium metal anodes," *Energy Storage Materials*, vol. 12, pp. 161–175, 2018.

[4] C. Wu, S. X. Dou, and Y. Yu, "The state and challenges of anode materials based on conversion reactions for sodium storage," *Small*, vol. 14, no. 22, p. 1703671, 2018.

[5] J. Kim, W. Jang, J. H. Kim, and C.-M. Yang, "Synthesis of graphene quantum dots-coated hierarchical CuO microspheres composite for use as binder-free anode for lithium-ion batteries," *Composites Part B: Engineering*, vol. 222, article 109083, 2021.

[6] P. Li, J. Y. Hwang, and Y.-K. Sun, "Nano/microstructured silicon–graphite composite anode for high-energy-density Li-ion battery," *ACS Nano*, vol. 13, pp. 2624–2633, 2019.

[7] K. Feng, M. Li, W. Liu et al., "Silicon-based anodes for lithium-ion batteries: from fundamentals to practical applications," *Small*, vol. 14, no. 8, p. 1702737, 2018.

[8] J. Lee, S.-A. Han, S.-M. Lee, M. S. Park, and J. H. Kim, "Electrochemical properties of nonstoichiometric silicon suboxide anode materials with controlled oxygen concentration," *Composites Part B: Engineering*, vol. 174, article 107024, 2019.

[9] Y. Zheng, J. Yang, J. Wang, and Y. NuLi, "Nano-porous Si/C composites for anode material of lithium-ion batteries," *Electrochimica Acta*, vol. 52, no. 19, pp. 5863–5867, 2007.

[10] B. Liu, Y. Jia, J. Li, H. Jiang, S. Yin, and J. Xu, "Multiphysics coupled computational model for commercialized Si/graphite composite anode," *Journal of Power Sources*, vol. 450, article 227667, 2020.

[11] M. K. Cho, S. J. You, J. G. Woo et al., "Anomalous Si-based composite anode design by densification and coating strategies for practical applications in Li-ion batteries," *Composites Part B: Engineering*, vol. 215, article 108799, 2021.

[12] L.-F. Cui, L. Hu, J. W. Choi, and Y. Cui, "Light-weight free-standing carbon nanotube-silicon films for anodes of lithium ion batteries," *ACS Nano*, vol. 4, no. 7, pp. 3671–3678, 2010.

[13] Y.-C. Zhang, Y. You, S. Xin et al., "Rice husk-derived hierarchical silicon/nitrogen-doped carbon/carbon nanotube spheres as low-cost and high-capacity anodes for lithium-ion batteries," *Nano Energy*, vol. 25, pp. 120–127, 2016.

[14] J. Ji, H. Ji, L. L. Zhang et al., "Graphene-encapsulated Si on ultrathin-graphite foam as anode for high capacity lithium-ion batteries," *Advanced Materials*, vol. 25, no. 33, pp. 4673–4677, 2013.

[15] S. Y. Kim, C. H. Kim, and C.-M. Yang, "Binder-free silicon anodes wrapped in multiple graphene shells for high- performance lithium-ion batteries," *Journal of Power Sources*, vol. 486, article 229350, 2021.

[16] H. Cheng, Z. Dong, C. Hu et al., "Textile electrodes woven by carbon nanotube–graphene hybrid fibers for flexible electrochemical capacitors," *Nanoscale*, vol. 5, no. 8, pp. 3428–3434, 2013.

[17] W. Yuan, Y. Zhang, L. Cheng, H. Wu, L. Zheng, and D. Zhao, "The applications of carbon nanotubes and graphene in advanced rechargeable lithium batteries," *Journal of Materials Chemistry A*, vol. 4, no. 23, pp. 8932–8951, 2016.

[18] J. Wu, X. Qin, H. Zhang et al., "Multilayered silicon embedded porous carbon/graphene hybrid film as a high performance anode," *Carbon*, vol. 84, pp. 434–443, 2015.

[19] J. Liu, "Charging graphene for energy," *Nature Nanotechnology*, vol. 9, no. 10, pp. 739–741, 2014.

[20] D. Y. Kim, J. H. Kim, M. Li et al., "Controllable pore structures of pure and sub-millimeter-long carbon nanotubes," *Applied Surface Science*, vol. 566, article 150751, 2021.

[21] D. Zhang, T. Yan, L. Shi, Z. Peng, X. Wen, and J. Zhang, "Enhanced capacitive deionization performance of graphene/carbon nanotube composites," *Journal of Materials Chemistry*, vol. 22, no. 29, pp. 14696–14704, 2012.

[22] H. Cui, X. Yan, M. Monasterio, and F. Xing, "Effects of various surfactants on the dispersion of MWCNTs–OH in aqueous solution," *Nanomaterials*, vol. 7, no. 9, p. 262, 2017.

[23] C. Ma, J. Jiang, Y. Han, X. Gong, Y. Yang, and G. Yang, "The composite of carbon nanotube connecting SnO_2/reduced graphene clusters as highly reversible anode material for lithium-/sodium-ion batteries and full cell," *Composites Part B: Engineering*, vol. 169, pp. 109–117, 2019.

[24] S. Y. Kim, K. S. Yang, and B.-H. Kim, "Improving the microstructure and electrochemical performance of carbon nanofibers containing graphene-wrapped silicon nanoparticles as a Li-ion battery anode," *Journal of Power Sources*, vol. 273, pp. 404–412, 2015.

[25] H. Hwang, C. H. Kim, J.-H. Wee, J. H. Han, and C.-M. Yang, "High-density graphene/single-walled carbon nanohorn composite supercapacitor electrode with high volumetric capacitance," *Applied Surface Science*, vol. 489, pp. 708–716, 2019.

[26] W.-S. Jeon, C. H. Kim, J.-H. Wee, J. H. Kim, Y. A. Kim, and C.-M. Yang, "Sulfur-doping effects on the supercapacitive behavior of porous spherical graphene electrode derived from layered double hydroxide template," *Applied Surface Science*, vol. 558, article 149867, 2021.

[27] C. H. Kim, C.-M. Yang, Y. A. Kim, and K. S. Yang, "Pore engineering of nanoporous carbon nanofibers toward enhanced supercapacitor performance," *Applied Surface Science*, vol. 497, article 143693, 2019.

[28] C. K. Chan, H. Peng, G. Liu et al., "High-performance lithium battery anodes using silicon nanowires," *Nature Nanotechnology*, vol. 3, no. 1, pp. 31–35, 2008.

[29] Q. Xiao, M. Gu, H. Yang et al., "Inward lithium-ion breathing of hierarchically porous silicon anodes," *Nature Communications*, vol. 6, no. 1, pp. 1–8, 2015.

[30] R. Andrews, E. Jacques, E. Qian, and E. C. Dickey, "Purification and structural annealing of multiwalled carbon nanotubes at graphitization temperatures," *Carbon*, vol. 39, no. 11, pp. 1681–1687, 2001.

[31] H. Richter, Z. Wang, and L. Ley, "The one phonon Raman spectrum in microcrystalline silicon," *Solid State Communications*, vol. 39, no. 5, pp. 625–629, 1981.

[32] M. Pimenta, G. Dresselhaus, M. S. Dresselhaus, L. G. Cançado, A. Jorio, and R. Saito, "Studying disorder in graphite-based systems by Raman spectroscopy," *Physical Chemistry Chemical Physics*, vol. 9, no. 11, pp. 1276–1290, 2007.

[33] J. Gao, W.-Y. Wang, L.-T. Chen, L. J. Cui, X. Y. Hu, and H. Z. Geng, "Optimizing processes of dispersant concentration and post-treatments for fabricating single-walled carbon nanotube transparent conducting films," *Applied Surface Science*, vol. 277, pp. 128–133, 2013.

[34] S. Y. Kim, J. Lee, B.-H. Kim, Y. J. Kim, K. S. Yang, and M. S. Park, "Facile synthesis of carbon-coated silicon/graphite spherical composites for high-performance lithium-ion batteries," *ACS Applied Materials & Interfaces*, vol. 8, no. 19, pp. 12109–12117, 2016.

[35] Š. Meškinis, A. Vasiliauskas, M. Andrulevičius, D. Peckus, S. Tamulevičius, and K. Viskontas, "Diamond like carbon films containing Si: structure and nonlinear optical properties," *Materials*, vol. 13, no. 4, p. 1003, 2020.

[36] X. Chen, X. Wang, and D. Fang, "A review on C1s XPS-spectra for some kinds of carbon materials," *Fullerenes, Nanotubes, and Carbon Nanostructures*, vol. 28, no. 12, pp. 1048–1058, 2020.

[37] M. Yoshio, H. Wang, K. Fukuda, T. Umeno, N. Dimov, and Z. Ogumi, "Carbon-coated Si as a lithium-ion battery anode material," *Journal of the Electrochemical Society*, vol. 149, no. 12, p. A1598, 2002.

[38] Y. Oumellal, N. Delpuech, D. Mazouzi et al., "The failure mechanism of nano-sized Si-based negative electrodes for lithium ion batteries," *Journal of Materials Chemistry*, vol. 21, no. 17, pp. 6201–6208, 2011.

[39] Q. Wei, G.-C. Liu, C. Zhang et al., "Novel honeycomb silicon wrapped in reduced graphene oxide/CNT system as high- stability anodes for lithium-ion batteries," *Electrochimica Acta.*, vol. 317, pp. 583–593, 2019.

[40] X. Tang, G. Wen, Y. Zhang, D. Wang, and Y. Song, "Novel silicon nanoparticles with nitrogen-doped carbon shell dispersed in nitrogen-doped graphene and CNTs hybrid electrode for lithium ion battery," *Applied Surface Science*, vol. 425, pp. 742–749, 2017.

[41] X. Ding, H. Wang, X. Liu et al., "Advanced anodes composed of graphene encapsulated nano-silicon in a carbon nanotube network," *RSC Advances*, vol. 7, no. 26, pp. 15694–15701, 2017.

[42] X. Gao, F. Wang, S. Gollon, and C. Yuan, "Micro silicon–graphene–carbon nanotube anode for full cell lithium-ion battery," *Journal of Electrochemical Energy Conversion and Storage*, vol. 16, no. 1, article 011009, 2019.

[43] H. Cai, K. Han, H. Jiang, J. Wang, and H. Liu, "Self-standing silicon-carbon nanotube/graphene by a scalable in situ approach from low-cost Al-Si alloy powder for lithium ion batteries," *Journal of Physics and Chemistry of Solids*, vol. 109, pp. 9–17, 2017.

[44] L. Xiao, Y.-H. Sehlleier, S. Dobrowolny et al., "Si–CNT/rGO nanoheterostructures as high-performance lithium-ion-battery anodes," *ChemElectroChem*, vol. 2, no. 12, pp. 1983–1990, 2015.

[45] B. Hu, X. Kuang, S. Xu, and X. Wang, "A novel anode with superior cycling stability based on silicon encapsulated in shell-like rGO/CNT architecture for lithium-ion batteries," *Energy Technology*, vol. 7, no. 5, p. 1801047, 2019.

[46] Z.-D. Huang, K. Zhang, T.-T. Zhang et al., "Binder-free graphene/carbon nanotube/silicon hybrid grid as freestanding anode for high capacity lithium ion batteries," *Composites Part A: Applied Science and Manufacturing*, vol. 84, pp. 386–392, 2016.

[47] X. Wang, K. Wen, T. Chen, S. Chen, and S. Zhang, "Supercritical fluid-assisted preparation of Si/CNTs@FG composites with hierarchical conductive networks as a high-performance anode material," *Applied Surface Science*, vol. 522, article 146507, 2020.

[48] X. Wang, G. Li, F.-M. Hassan et al., "Building sponge-like robust architectures of CNT–graphene–Si composites with enhanced rate and cycling performance for lithium-ion batteries," *Journal of Materials Chemistry A*, vol. 3, no. 7, pp. 3962–3967, 2015.

[49] X. Liu, X. Zhu, and D. Pan, "Solutions for the problems of silicon–carbon anode materials for lithium-ion batteries," *Royal Society Open Science*, vol. 5, article 172370, 2018.

[50] J. Niu, S. Zhang, Y. Niu et al., "Direct amination of Si nanoparticles for the preparation of Si@ultrathin SiO_x@graphene nanosheets as high performance lithium-ion battery anodes," *Journal of Materials Chemistry A*, vol. 3, no. 39, pp. 19892–19900, 2015.

[51] S. J. Lee, Y. S. Joe, J. S. Yeon et al., "Hierarchically structured silicon/graphene composites wrapped by interconnected carbon nanotube branches for lithium-ion battery anodes," *International Journal of Energy Research*, vol. 46, no. 11, pp. 15627–15638, 2022.

[52] Y. Joshi, S. Zamani, C. Klaassen, and Y. L. Joo, "Mitigation and in situ probing of volume expansion in silicon/graphene hybrid anodes for high-capacity, high-rate-capable lithium-ion batteries," *Advanced Energy and Sustainability Research*, vol. 2, no. 12, article 2100125, 2021.